


Article

Aboveground Carbon Stock Estimation Based on Backpack LiDAR and UAV Multispectral Imagery at the Forest Sample Plot Scale

Rina Su ^{1,2} , Wala Du ^{1,3,*}, Yu Shan ⁴, Hong Ying ⁴, Wu Rihan ⁴ and Rong Li ⁴¹ The Institute of Grassland Research of CAAS, Hohhot 010010, China; 20172104185@mails.imnu.edu.cn² College of Resource and Environmental Sciences, Inner Mongolia Agricultural University, Hohhot 010018, China³ Forest and Grassland Disaster Prevention and Litigation Field Scientific Observation and Research Station of Inner Mongolia Autonomous Region, Arshan 137400, China⁴ The College of Geographic Science, Inner Mongolia Normal University, Hohhot 010022, China; yushan@imnu.edu.cn (Y.S.); hongy864@nenu.edu.cn (H.Y.); wurh651@imnu.edu.cn (W.R.); 20224016019@mails.imnu.edu.cn (R.L.)

* Correspondence: duwala@caas.cn; Tel.: +86-186-8602-5858

Abstract: Aboveground carbon stocks (AGCs) in forests play an important role in understanding carbon cycle processes. The global forestry sector has been working to find fast and accurate methods to estimate forest AGCs and implement dynamic monitoring. The aim of this study was to explore the effects of backpack LiDAR and UAV multispectral imagery on AGC estimation for two tree species (*Larix gmelinii* and *Betula platyphylla*) and to emphasize the accuracy of the models used. We estimated the AGC of *Larix gmelinii* and *B. platyphylla* forests using multivariate stepwise linear regression and random forest regression models using backpack LiDAR data and multi-source remote sensing data, respectively, and compared them with measured data. This study revealed that (1) the diameter at breast height (DBH) extracted from backpack LiDAR and vegetation indices (RVI and GNDVI) extracted from UAV multispectral imagery proved to be extremely effective in modeling for estimating AGCs, significantly improving the accuracy of the model. (2) Random forest regression models estimated AGCs with higher precision (Xing'an larch $R^2 = 0.95$, RMSE = 3.99; white birch $R^2 = 0.96$, RMSE = 3.45) than multiple linear regression models (Xing'an larch $R^2 = 0.92$, RMSE = 6.15; white birch $R^2 = 0.96$, RMSE = 3.57). (3) After combining backpack LiDAR and UAV multispectral data, the estimation accuracy of AGCs for both tree species (Xing'an larch $R^2 = 0.95$, white birch $R^2 = 0.96$) improved by 2% compared to using backpack LiDAR alone (Xing'an larch $R^2 = 0.93$, white birch $R^2 = 0.94$).

Keywords: backpack LiDAR; UAV multispectral imagery; aboveground carbon stock (AGC); multiple stepwise linear regression (MSLR); random forest regression (RF)



Citation: Su, R.; Du, W.; Shan, Y.; Ying, H.; Rihan, W.; Li, R. Aboveground Carbon Stock Estimation Based on Backpack LiDAR and UAV Multispectral Imagery at the Forest Sample Plot Scale. *Remote Sens.* **2024**, *16*, 3927. <https://doi.org/10.3390/rs16213927>

Academic Editors: Qinghua Guo and Brenden E. McNeil

Received: 4 September 2024

Revised: 28 September 2024

Accepted: 18 October 2024

Published: 22 October 2024



Copyright: © 2024 by the authors. Licensee MDPI, Basel, Switzerland. This article is an open access article distributed under the terms and conditions of the Creative Commons Attribution (CC BY) license (<https://creativecommons.org/licenses/by/4.0/>).

1. Introduction

Forest ecosystems play a crucial role in terrestrial ecosystems, acting as massive global carbon reservoirs that contain 80% of the terrestrial carbon stored in aboveground biomass [1]. The aboveground carbon stock (AGC) of forests is a key parameter for assessing the carbon sequestration capacity and carbon balance above the forest soil layer, making it vital to understand the role of forests in carbon cycling and climate change [2]. As the issue of climate change becomes increasingly severe, accurately estimating and monitoring changes in forest AGCs are essential for developing sustainable ecosystem management and policies to mitigate climate change [3].

However, accurately estimating forest AGCs is a challenging task. Although traditional field survey methods are precise and reliable, they are time-consuming and labor-intensive, making it difficult to apply them over large areas or to fully cover diverse ecosystem

types. As a result, remote sensing-assisted datasets have gradually become an important supplementary approach, providing spatially and temporally continuous information over extensive regions [4]. Remote sensing data sources such as LiDAR and UAV multispectral imagery have high-resolution and wide-area surface information, offering the possibility of estimating carbon stocks over large areas [5–8]. However, despite numerous studies showing that LiDAR or optical data alone can predict forest AGCs, the accuracy obtained from these methods without support from field measurements remains a challenge. Therefore, calibration and validation of remote sensing-assisted prediction techniques still require field measurement data.

Light detection and ranging (LiDAR) data, as a remote sensing data source, can be used to rapidly and accurately obtain elevation information and vertical structure data for vegetation cover [9] and are among the latest remote sensing technologies for forest carbon accounting [10]. Backpack LiDAR, such as LiBackpack, a new type of portable LiDAR, offers high capacity, accessibility, and flexibility in route selection and can obtain high-quality 3D dense point clouds in forests with different vegetation structures [11]. However, despite the accuracy of backpack LiDAR for measuring tree diameter [12,13], identifying the best variables suitable for different tree species remains challenging, especially in the absence of canopy spectral information, where LiDAR data classification accuracy for tree species under complex vegetation conditions is limited [14]. On the other hand, UAV multispectral imagery includes multispectral information, aiding in studying the spectral characteristics of different tree species. Early research revealed that the high-resolution image texture features of optical remote sensing data are strongly correlated with forest biomass [15,16], and the vegetation indices obtained from optical data typically reach saturation at relatively low biomass values [17,18]. UAV multispectral imagery has better spatial, spectral, and temporal resolution compared to other optical datasets for similar data volumes and data collection costs [19], and their time-series data provide high-quality information on seasonal changes in forests. Additionally, UAV multispectral data are effectively used for forest resource monitoring and dynamic management [20]. Recent studies suggest that combining LiDAR and optical sensors is a feasible approach for estimating biomass and carbon storage in both plantations and natural forests [21]. Brown et al. [22] showed that modeling with a large amount of field measurement data added to data fusion can improve the estimation of forest AGBs and AGCs. Kim et al. [23] stated that combining spectral information with attributes derived from LiDAR data is more suitable for assessing the AGB and AGC than using optical images or LiDAR data alone. However, finding a method for accurately estimating forest AGCs with fewer field measurements to establish regression models is currently challenging.

Extracting vegetation information from remote sensing imagery and integrating it with ground-measured data for modeling has become an effective and popular method for obtaining regional forest AGCs. The study mentioned the use of parametric and non-parametric models. Multiple stepwise linear regression (MSLR) represents the traditional parametric model, assuming a linear relationship between predictive variables and the variable being predicted. However, this assumption limits the inherent nonlinearity of the relationship between them and requires a large sample size [24]. On the other hand, random forest regression (RF) is a nonparametric model that does not assume a specific distribution for the samples. It can handle complex nonlinear relationships and high-dimensional problems and has been proven effective for estimating forest AGCs [25]. Additionally, machine learning techniques aid in combining data from different sources to improve outcomes [26].

In this study, *L. gmelinii* and *B. platyphylla*, two typical tree species, were chosen as the study species due to their ecological significance and notable differences in carbon storage [27]. Liu et al. explored the carbon storage capacity of Xing'an larch and birch forests, suggesting that they have an important role in boreal forests [28]. *Larix gmelinii*, an important economic tree species, grows in cold and dry conditions and has a high carbon stock. In contrast, compared with *L. gmelinii*, *B. platyphylla* plays a different role in ecosystems and has distinct growth environments and characteristics, leading to potentially

significant differences in carbon storage. By studying these two typical species, we aim to deepen the understanding of the variability in forest carbon storage among different tree species, thereby providing more accurate estimation models to support forest resource management and conservation.

Despite these developments, comprehensive validation of the accuracy of forest AGC estimation is lacking. This study is dedicated to addressing this challenge. We hypothesize that the combination of forest vertical variables with horizontal variables from optical images through allometric relationships can be used to accurately estimate forest AGCs at the plot scale with minimal field measurement data. Therefore, the objectives of this study are: (1) to assess the effectiveness of using backpack LiDAR and UAV multispectral imagery in estimating aboveground carbon stocks (AGC) for *L. gmelinii* and *B. platyphylla*; (2) to compare the predictive accuracy of different models; and (3) to validate whether integrating multi-source data can enhance the accuracy of AGC estimation.

2. Materials and Methods

2.1. Study Area

The research area is located in the Dural National Forest Farm, Arxan city, Hinggan League, Inner Mongolia Autonomous Region of China (119°28′–120°01′E, 47°15′–47°35′N), which is a comprehensive forest farm integrating both natural and artificial forests (Figure 1—Some of the sampling sites are located outside of the yellow box labeled as the UAV-LS working area. However, in the actual study, the sample plots used in the estimation of AGCs were those within the yellow boxes). This region, situated in the Hinggan League of the Inner Mongolia Autonomous Region of China, is an important natural ecological conservation area. The total area of the Dural Forest Farm is 49,812 hectares, 33,466 hectares of which are designated for forestry, accounting for 67% of the total area. The forest coverage rate is as high as 48.3%, with an altitude ranging from 792 to 1495 metres. The region experiences a cold temperate continental monsoon climate, with an average annual temperature of 1.48 °C, an average temperature of −25.6 °C in the coldest month, and an average temperature of 16.6 °C in the hottest month. The average annual precipitation is 437 mm. The main tree species of the forest are *B. platyphylla* and *L. gmelinii*, along with a minority of *Populus davidiana* and *Pinus sylvestris*. Most of the area has good site conditions, with similar forest types distributed in concentrated and contiguous areas, which is beneficial for forest management and operation [29].

2.2. Inventory Data

Within the study area covered by airborne LiDAR data, we conducted two field surveys for tree information collection at the plot scale in July 2021 and July 2022 (Figure 2). In this study, we used field-measured data from 435 rectangular plots, each measuring 0.04 ha (230 plots from larch forests and 205 plots from birch forests). Additionally, considering the distributions of *L. gmelinii* and *B. platyphylla*, these plots were established to provide a good statistical representation of these two main tree species. Given the relative rareness of tree species in the study area, our data collection specifically targeted these two tree species. Within each plot, the tree heights were measured using a laser rangefinder. Trees with a diameter at breast height (DBH) greater than 5 cm were marked at a height of 1.2 m using a DBH measuring tape. Simultaneously, the coordinates of the plot's center point and its four corners were obtained using a GNSS receiver with differential satellite station technology, which was employed for accurate positioning.

Currently, most forest biomass estimation studies are based on existing allometric growth equations selected according to the study area or equations fitted from the analysis of felled trees [30]. Allometric growth equations are fundamental not only for calculating the biomass of various tree organs and vegetation carbon storage but also for estimating tree carbon sequestration rates and potentials [31]. The diameter at breast height (DBH) and tree height (H) have been used as predictive variables for estimating aboveground biomass (AGB) [32,33]. Therefore, this study estimated the AGB of individual *L. gmelinii*

and *B. platyphylla* trees in the Dural Forest Farm based on DBH (cm) and H using allometric growth equations for the dominant tree species of the Greater Khingan Range in Inner Mongolia [34,35] (Table 1). The total AGB of the forests in the study area was calculated as shown in Equation (1):

$$AGB_{Total} = W_{Stem} + W_{Branch} + W_{Leaf} + W_{Bark} \quad (1)$$

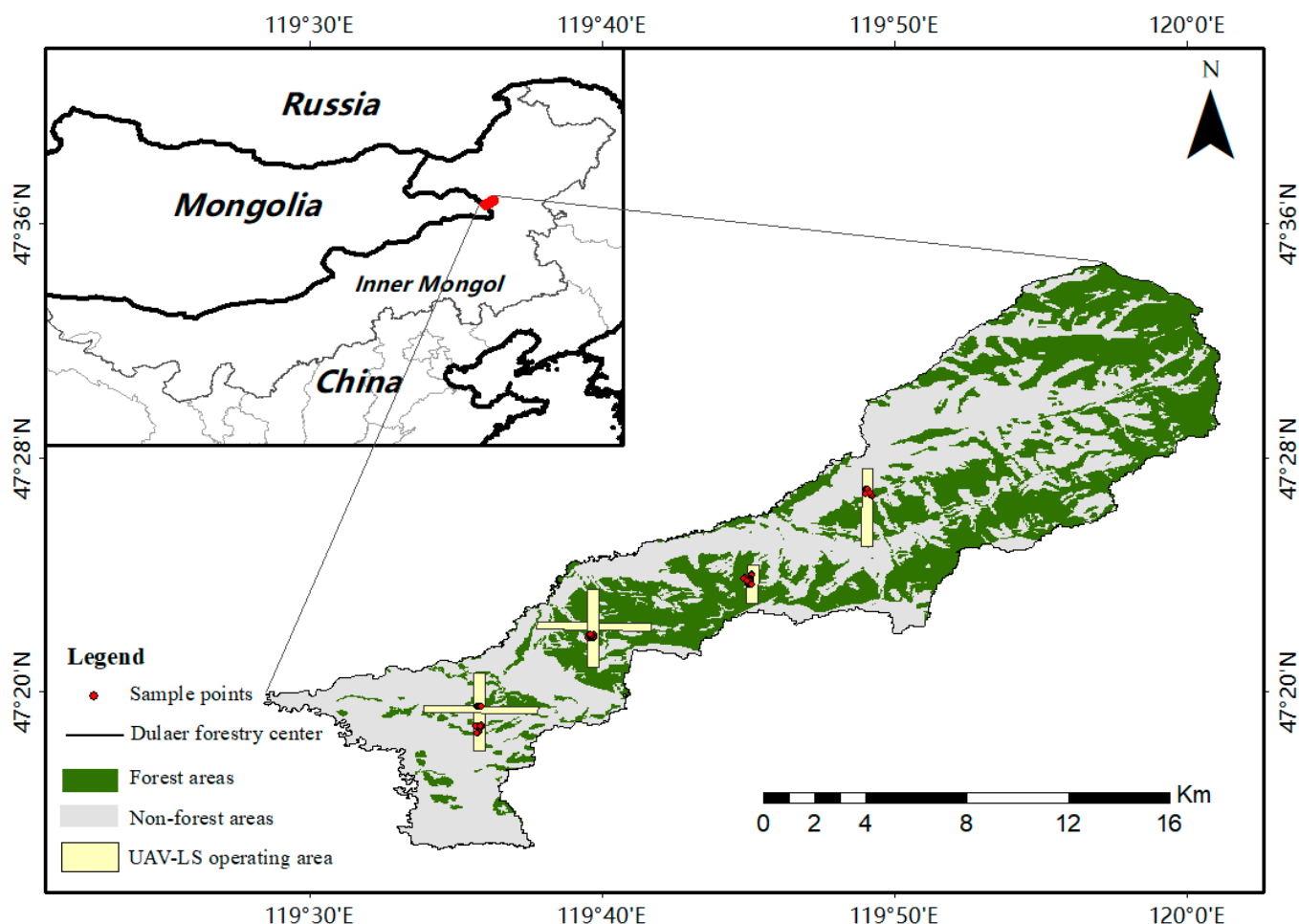


Figure 1. Location of the study area. The study area is located entirely within Chinese territory, with research activities strictly confined to ecological and environmental aspects.

Table 1. Allometric growth equations for Inner Mongolia *L. gmelinii* and *B. platyphylla*.

Organ	Allometric Growth Equation of <i>Larix gmelinii</i>	Allometric Growth Equation of <i>Betula platyphylla</i>
Stem	$W_{Stem} = 0.01258(D^2H)^{0.99331}$	$W_{Stem} = 0.02853(D^2H)^{0.89278}$
Branch	$W_{Branch} = 0.00136(D^2H)^{1.02797}$	$W_{Branch} = 0.00278(D^2H)^{1.02568}$
Leaf	$W_{Leaf} = 0.01009(D^2H)^{0.64543}$	$W_{Leaf} = 0.01545(D^2H)^{0.61265}$
Bark	$W_{Bark} = 0.002307(D^2H)^{0.70655}$	$W_{Bark} = 0.02392(D^2H)^{0.71131}$

D represents the diameter at breast height (DBH) of the tree; H represents the tree height; W_{Stem} represents the biomass of the tree trunk; W_{Branch} represents the biomass of the branches; W_{Leaf} represents the biomass of the leaves; and W_{Bark} represents the biomass of the bark.

For the *L. gmelinii* and *B. platyphylla* forests in the Dural Forest Farm, we referred to the standard conversion factors for *L. gmelinii* and *B. platyphylla* forests in the Greater Khingan Range, which are 0.4948 and 0.5018, respectively [36], to convert AGB to AGC

(aboveground carbon) [37], as shown in Equations (2) and (3). Table 2 provides a summary of the forest parameters obtained from field measurements.

$$AGC_{Larix} = 0.4948 \times AGB_{Total} \quad (2)$$

$$AGC_{Betula} = 0.5018 \times AGB_{Total} \quad (3)$$



Figure 2. Parameter measurements in the study area: (a) Setup of base stations. (b) Tree height measurement. (c) Obtaining the coordinates. (d) DBH measurement and recording.

In the formula, AGB_{Total} represents the total aboveground biomass, AGC_{Larix} is the aboveground carbon stock of *L. gmelinii*, and AGC_{Betula} is the aboveground carbon stock of *B. platyphylla* forests.

After simplifying Equations (1)–(3), the final equations for calculating the measured aboveground carbon (AGC) for *L. gmelinii* and *B. platyphylla* forests are obtained, as shown in Equations (4) and (5):

$$AGC_{Larix_Measured} = 0.0248 \times (D^2H)^{0.8955} \quad (4)$$

$$AGC_{Betula_Measured} = 0.034 \times (D^2H)^{0.8622} \quad (5)$$

In the formulas, AGC_{Larix} measured represents the measured aboveground carbon stock of *L. gmelinii*; AGC_{Betula} measured represents the measured aboveground carbon stock of *B. platyphylla* forests; D is the measured diameter at breast height (DBH); and H is the measured tree height.

Table 2. Summary statistics of the field-measured forest parameters.

Variable	<i>Larix gmelinii</i>				<i>Betula platyphylla</i>			
	Min	Max	Mean	Std	Min	Max	Mean	Std
H (m)	4	16	11.89	2	6	16.9	13.43	2.25
DBH (cm)	5.5	35	15	4.28	5.3	29.8	12.58	4.37
AGB (Kg)	3950	320,540	64,490	40,480	6590	231,500	56,580	39,570
AGC (Kg)	1960	158,610	31,910	20,030	3310	116,170	28,390	19,850

2.3. Remote Sensing Data

2.3.1. Backpack LiDAR Data

The Backpack Laser Scanning (BLS) system is a backpack-mounted device that integrates LiDAR with other sensors. The simultaneous localization and mapping (SLAM) algorithm allows for the rapid and continuous acquisition of LiDAR point cloud data, even as the robot or device moves through an unknown environment. The SLAM algorithm enables a robot or device to autonomously create a map and accurately locate itself without knowing its initial position, facilitating navigation in unknown environments.

In this study, we employed the LiBackpack DGC 50 backpack laser scanner developed by Beijing Greenvalley Technology Co., Ltd. (Beijing, China) (Figure 3). This device efficiently captures tree point cloud data within plots using a designed “S”-shaped hiking route for data collection [38]. The choice of the LiBackpack DGC 50 was based on its effective data collection capability and reliable data quality assurance. During data collection, the operator connects to the backpack laser scanner via a smartphone to monitor the number of satellite signals and real-time point cloud scanning status. To ensure the quality of the point cloud data, steady movement is required during collection, especially at turns, to ensure data accuracy and completeness.

To acquire point cloud data with geographic coordinates, a GNSS receiver (CHC iRTK 5) is used in an open area outside the plot with stable Global Navigation Satellite System signals. This receiver acquires the absolute geographic coordinates of a point using satellite differential techniques, and a base station is set up at this point to gather static data. Finally, the raw point cloud data, trajectory files, and GNSS static data are imported into GreenValley International Li-Fuser BP software (Digital Green Earth; Beijing, China) for processing to obtain point cloud data with absolute geographic location information.

The LiBackpack DGC 50 laser scanner and Li-Fuser BP software were selected for their superior capabilities in rapid data acquisition and processing. The backpack LiDAR data were collected by an operator who walked along an ‘S’-shaped route, ensuring comprehensive coverage of each plot. During data collection, the operator monitored the data quality in real-time via a mobile connection, ensuring the accuracy and completeness of the point cloud data. The scanning path was meticulously designed to cover the entirety of each designated plot, ensuring that the collected data was precisely aligned with the AGC measurement points.

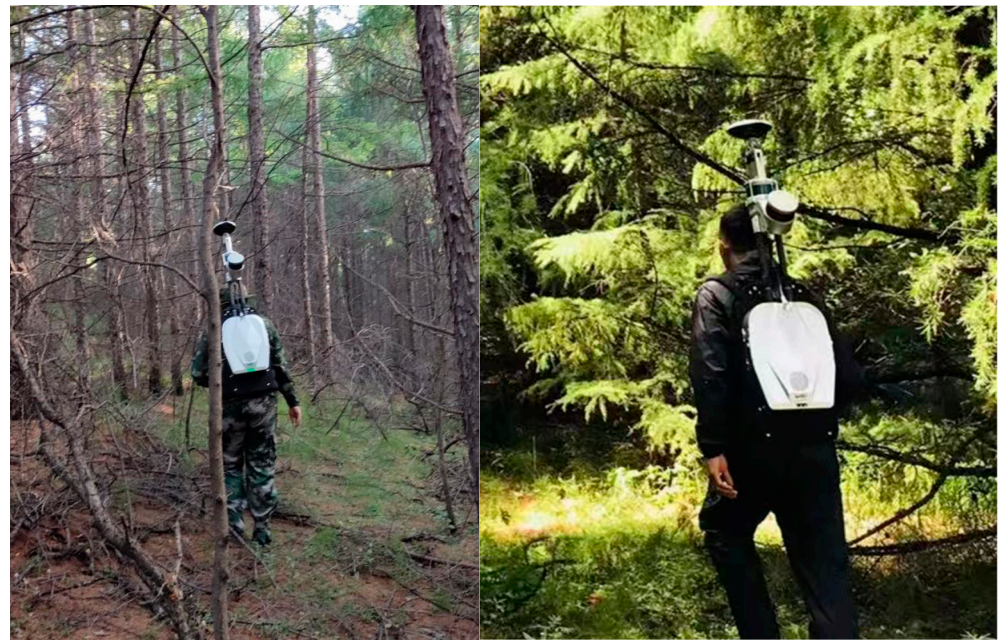


Figure 3. LiBackpack DGC50 backpack LiDAR scanning system.

When processing the backpack LiDAR data, the initial steps involve copying the raw field data and exporting the image data. Next, Hi-Target Business Center software (Beijing Huatai Kejie Information Technology Co.; Beijing, China) is used to convert the static data into GNSS files in RINEX format. The Insta360 studio software (Shenzhen Qianhai Shadowstone Innovative Technology Co.; Shenzhen, China) is then utilized to convert the required video format from the backpack LiDAR into .MP4. Afterward, Li-Fuser BP software is used to process the data coordinates, calibrating the relative coordinates from the mobile trajectory to the geodetic coordinates, with all coordinates resolved using the CGCS2000 3-degree GK CM 120E system (Environment System Research Institute, ESRI). Each plot covers an area of 0.04 hectares, and the LiDAR scan ensures comprehensive coverage of all trees, providing complete data on tree height, DBH, and canopy structure.

The processed Backpack data were preprocessed using LiDAR360 V5.3 software (Digital Green Earth Ltd.; Beijing, China). The point cloud data were clipped according to the sample range, and after removing redundancy and noise, the data were filtered. The ground points were classified, and a digital elevation model (DEM) was generated through irregular triangular mesh interpolation. Based on the DEM, the point cloud was normalized to obtain seed points, and individual trees were segmented using these seed points to acquire ground-based point cloud data. Figures 4 and 5 display the profile point cloud data of the collected *L. gmelinii* and *B. platyphylla* plots, visualized by elevation.

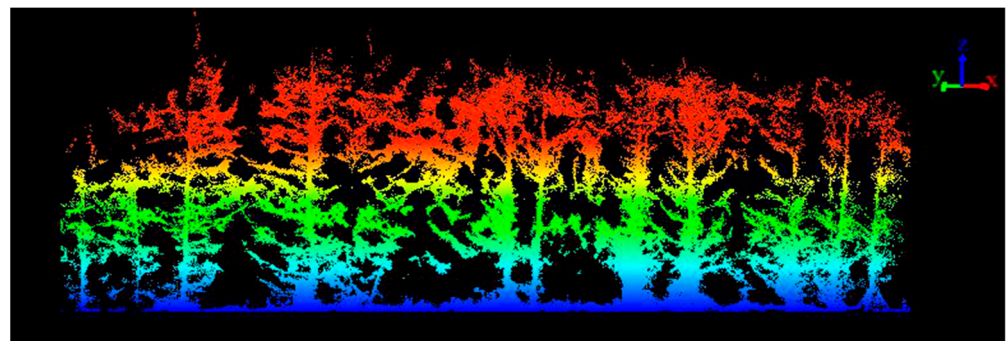


Figure 4. Point cloud data of *L. gmelinii* sample plot profiles collected via backpack LiDAR.

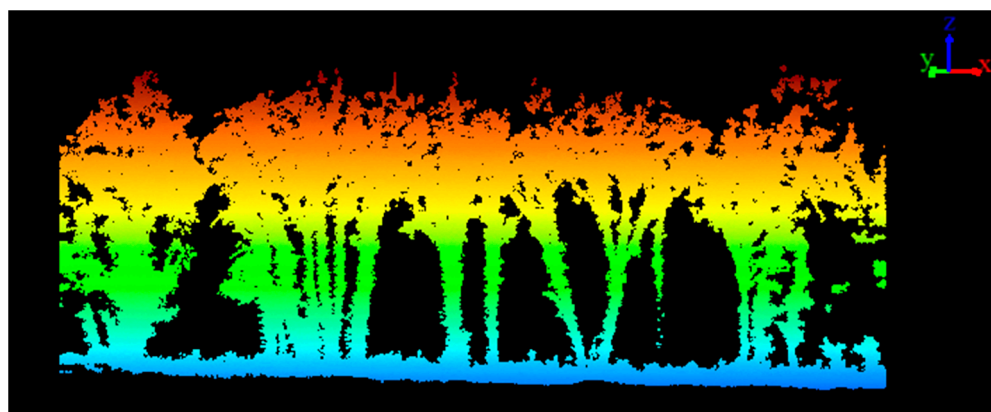


Figure 5. Point cloud data of *B. platyphylla* sample plot profiles collected by backpack LiDAR.

2.3.2. UAV Multispectral Data

On 11 July 2021, multispectral imagery was collected across six transect areas using a Feima D200 multirotor UAV (Pegasus Robotics Technology Co.; Shenzhen, China) and a V300 fixed-wing UAV equipped with a D-CAM2000 multispectral sensor (Pegasus Robotics Technology Co.; Shenzhen, China) (shown in Figure 6). The sensor captured six spectral bands, namely blue, green, red, red-edge, near-infrared, and panchromatic bands. The flight operation was designed at an altitude of 383 m with an 80% flight path overlap and 60% side overlap. The UAVs were equipped with an inertial navigation system (IMU), providing a spatial resolution of 0.02 m. The acquired sensor images were loaded into pix4dmapper 4.5.6 official version software (Pix4D Company, Switzerland) to allow the feature point matching algorithm to match the different images, and the aerial triangulation method and beam method leveling algorithm were used to obtain the multispectral images of the UAV-piloted flight area. During field data collection, we used RTK-GNSS equipment to precisely measure the corner and center points of each plot, ensuring centimeter-level accuracy in the coordinates. These coordinates were then converted to the same coordinate system as the UAV imagery (CGCS2000) to maintain spatial consistency across different data sources. In ArcMap 10.7, the UAV-acquired multispectral images were cropped according to the boundaries of each plot, ensuring that the resulting images only included pixels within the plot area. Additionally, feature point matching algorithms were applied to spatially align the UAV imagery with ground-based data and further optimized using bundle adjustment techniques to ensure precise spatial correspondence between datasets.

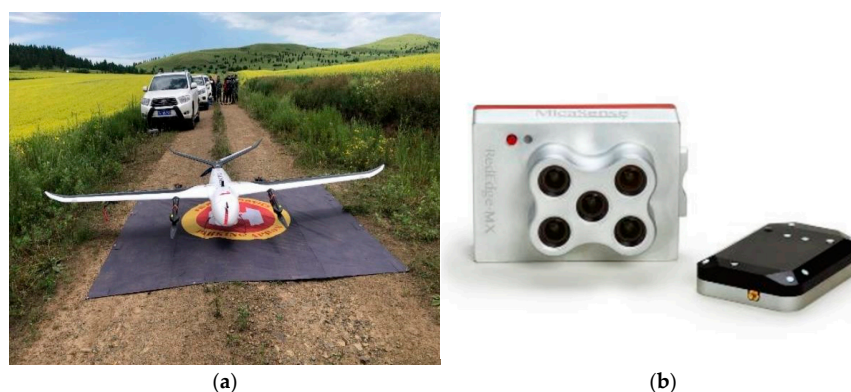


Figure 6. (a) Pegasus V300 drone and (b) multispectral D-CAM2000 sensor.

The six spectral bands of UAV multispectral imagery contain rich vegetation information, which are crucial factors in estimating forest carbon storage. This study selected five bands closely related to vegetation (blue, green, red, and near-infrared) and used ArcGIS 10.7 to extract band information for the main tree species plots in the study area.

The spectral information resulting from the reflection, absorption, and scattering of solar radiation by the forest canopy, along with chlorophyll content, is an important variable for AGB/AGC modeling [39–41]. The seven vegetation indices derived from band combinations, including NDVI, RVI, DVI, EVI, GNDVI, NDRE, and SAVI, effectively reflect vegetation growth and health and are closely related to AGB/AGC [42–48]. In this study, these vegetation indices were extracted and coupled with LiDAR structural variables to establish a model for quantitatively estimating AGC density (see Table 3). ENVI 5.3 software was used to perform calculations on the aforementioned bands of UAV multispectral imagery, computing various types of vegetation indices for modeling and analysis when estimating forest vegetation carbon storage.

Table 3. Vegetation Index Formulas.

Vegetation Index	Descriptions	Equations	References
NDVI	Normalized Vegetation Index	$NDVI = \frac{\rho_{NIR} - \rho_{RED}}{\rho_{NIR} + \rho_{RED}}$	[42]
RVI	Ratio Vegetation Index	$RVI = \frac{\rho_{NIR}}{\rho_{RED}}$	[43]
DVI	Difference Vegetation Index	$DVI = \rho_{NIR} - \rho_{RED}$	[44]
EVI	Enhanced Vegetation Index	$EVI = \frac{2.5 \times (\rho_{NIR} - \rho_{RED})}{(\rho_{NIR} + 6 \times \rho_{RED} - 7.5 \times \rho_{BLUE} + 1)}$	[45]
GNDVI	Green Normalized Vegetation Index	$GNDVI = \frac{\rho_{NIR} - \rho_{GREEN}}{\rho_{NIR} + \rho_{GREEN}}$	[46]
NDRE	Normalized Redside Vegetation Index	$NDRE = \frac{\rho_{RedEdge} - \rho_{NIR}}{\rho_{RedEdge} + \rho_{NIR}}$	[47]
SAVI	Soil-Adjusted Vegetation Index	$SAVI = 1.5 \times \frac{(\rho_{NIR} - \rho_{RED})}{(\rho_{NIR} + \rho_{RED} + 0.5)}$	[48]

2.4. Predictive Model

Forest AGC was estimated using combinations of three types of data variables: LiDAR variables (LVs), optical variables (OVs), and a combination of LiDAR and optical variables (LVs + OVs). Predictive variables from LiDAR data (2 variables) and vegetation index data (7 variables) were used along with corresponding AGC field data to estimate the forest AGC of *L. gmelinii* and *B. platyphylla*. The models were run with the measured forest AGC and remotely sensed data-derived indices as dependent and independent variables, respectively. The impact of different modeling methods on result quality varies [49]. In this study, two types of multiple stepwise linear regression (MSLR) models and random forest (RF) regression models were used to predict AGCs.

2.4.1. Multiple Stepwise Linear Regression Model

A multiple linear regression model using a stepwise selection of predictive variables was employed to predict the relationship between AGCs obtained from remote sensing datasets and variables. Stepwise regression is a parametric algorithm that screens variables and establishes an optimal regression equation. In the stepwise regression modeling process, predictive variables are input into the regression equation one by one based on given statistical standards. In each step of the analysis, the variable with the highest correlation with the dependent variable is first entered into the regression equation, followed by the introduction of other variables one by one to establish the model. The MSLR model has been widely applied in the estimation of forest AGB and AGCs [50–53].

However, these techniques are not conducive to establishing complex relationships between biophysical parameters and remote sensing matrices. Machine learning technology is a powerful nonlinear regression method that can serve as an alternative to traditional methods for dealing with complex and nonlinear problems. Machine learning algorithms can integrate data from different sources [26].

2.4.2. Random Forest Regression Model

The random forest (RF) method is a classification and regression method that uses regression trees to predict the relationships between variables and is widely used in biomass carbon storage prediction [54,55]. It is often effective in predictive models [56]. In this

algorithm, a subset of training data is randomly selected to construct a decision tree. The remaining part of the training data is used to estimate the error of each tree. At each node of the tree, a set of predictive variables is randomly selected to determine the split. Hundreds of trees are constructed in a similar manner, and the final prediction is formed by aggregating the predicted values of all the trees [19]. RF has been proven to reduce overfitting and systematic errors [57], rank important variables, and generate independent measurements of prediction error [58]. It has been shown to be more accurate than linear regression models [59].

In this study, the Random Forest (RF) model utilized data from 210 Xing'an larch and 180 white birch trees, selecting one-third of the total number of variables (70 for larch and 60 for birch) as the basis for splitting at each node. The input data consisted of structural attributes derived from LiDAR, such as diameter at breast height (DBH) and tree height (H), along with vegetation indices extracted from UAV multispectral imagery, including the Ratio Vegetation Index (RVI) and Green Normalized Difference Vegetation Index (GNDVI). The model was trained and validated using a 70/30 split ratio, with cross-validation employed to ensure the robustness and stability of the model's performance. Model accuracy was evaluated through multiple metrics, including the root mean square error (RMSE), coefficient of determination (R^2), and mean absolute error (MAE). Furthermore, the model assessed the relative importance of each variable by measuring the increase in prediction error when a particular variable was omitted, which facilitated model optimization and highlighted the most influential predictors.

2.5. Accuracy Evaluation

To validate the effectiveness of the models, in this study, we randomly selected 160 plots from 230 field-measured *L. gmelinii* carbon storage plots and 144 plots from 205 field-measured *B. platyphylla* carbon storage plots to construct regression models. The remaining 70 and 61 plots were used to evaluate the predictive accuracy of our established forest AGC estimation models. Widely used statistical indicators were employed to assess the accuracy of the forest AGC estimation models. For each model, we calculated the coefficient of determination (R^2 , Formula (6)), root mean square error (RMSE, Formula (7)), relative root mean square error (RRMSE, Formula (8)), and mean absolute error (MAE, Formula (9)). R^2 measures the fit between the predicted and observed values, while RMSE, RRMSE, and MAE calculate the estimation error of the model. A larger R^2 indicates a better fit between the observed and predicted values. Smaller RMSE, RRMSE, and MAE values indicate smaller estimation errors in the model. The calculation formulas are as follows:

$$R^2 = 1 - \frac{\sum_{i=1}^n (y_i - \hat{y}_i)^2}{\sum_{i=1}^n (y_i - \bar{y})^2} \quad (6)$$

$$RMSE = \sqrt{\frac{\sum_{i=1}^n (\hat{y}_i - y_i)^2}{n}} \quad (7)$$

$$RRMSE = \frac{RMSE}{\bar{y}} \times 100 \quad (8)$$

$$MAE = \frac{\sum_{i=1}^n |y_i - \hat{y}_i|}{n} \quad (9)$$

In the formulas, n represents the number of samples; y_i and \hat{y}_i are the observed and predicted AGC values, respectively, for the i -th sample; and \bar{y} is the average AGC value of the i -th sample.

3. Results

3.1. Extraction of Forest Structural Parameters Based on Remote Sensing Data

First, we conducted sampling at the field site, where each tree within the plot was scanned using backpack LiDAR. The data were then exported and processed in LiDAR360

software, where the point cloud data underwent cropping, filtering, ground point classification, normalization, and individual tree segmentation. This process ultimately provided the DBH and H of trees with specific coordinates. Finally, the DBH and H measured in the field were fitted and cross-validated with those extracted from the backpack LiDAR data.

Figure 7a shows the comparison between the measured DBH and the DBH extracted from the Backpack LiDAR for the *Larix gmelinii* forest plot ($R^2 = 0.9966$, RMSE = 0.25, and MAE = 0.17). Figure 7b presents the comparison between the measured H and the H extracted from the Backpack LiDAR for the *Larix gmelinii* forest plot ($R^2 = 0.4507$, RMSE = 1.48, and MAE = 3.15).

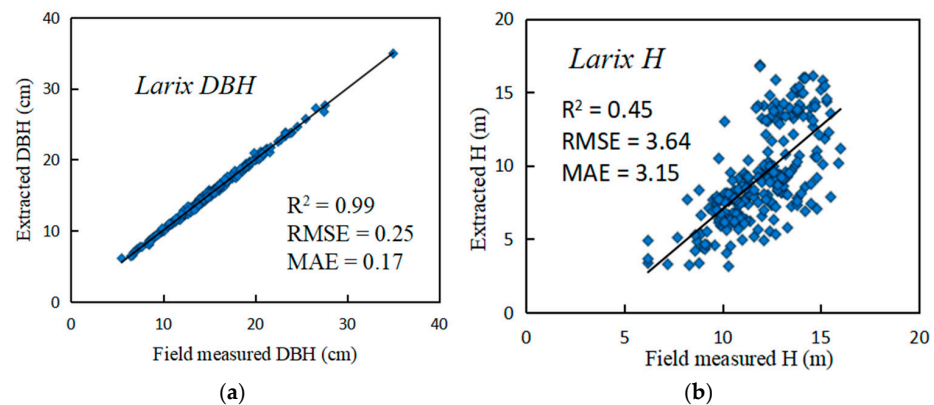


Figure 7. (a) Comparison of measured DBH with DBH extracted by backpack LiDAR in Larix; (b) Comparison of measured DBH with DBH extracted by backpack LiDAR in Larix.

Figure 8a shows the comparison between the measured DBH and the DBH extracted from the Backpack LiDAR for the *Betula platyphylla* forest plot ($R^2 = 0.984$, RMSE = 0.51, and MAE = 0.37). Figure 8b presents the comparison between the measured H and the H extracted from the Backpack LiDAR for the *Betula platyphylla* forest plot ($R^2 = 0.6227$, RMSE = 1.51, and MAE = 1.61).

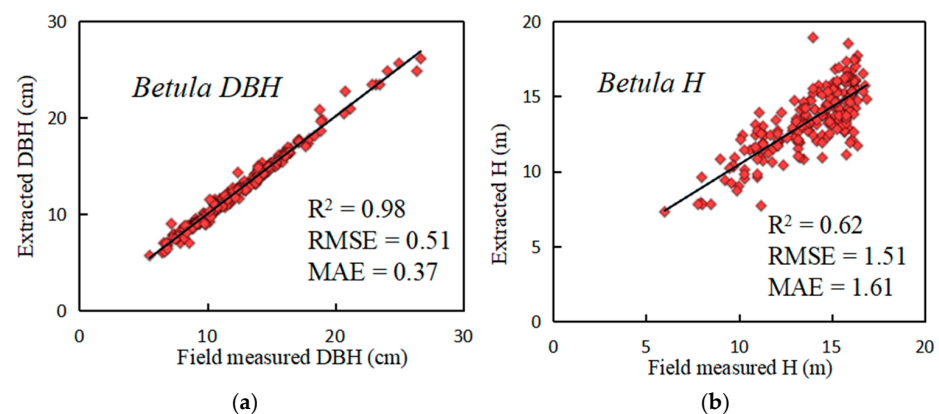


Figure 8. (a) Comparison of measured DBH with DBH extracted by backpack LiDAR in Betula; (b) Comparison of measured DBH with DBH extracted by backpack LiDAR in Betula.

3.2. Aboveground Carbon Stock Estimation in Forests at the Sample Plot Scale Based on LiDAR Remote Sensing Data

3.2.1. Aboveground Carbon Stock Estimation in Forests Based on LiDAR Remote Sensing Using Multiple Stepwise Linear Regression Methods

The modeling approach used a simple regression fitting method to model LiDAR-estimated DBH and H with forest AGC. We used model accuracy evaluation metrics (such as R^2 and RMSE) to test the significance of the model to eliminate variables that have an insignificant impact on the dependent variable. Finally, we established a multivariate

linear regression equation containing all important variables to explain the variation in the dependent variable. Therefore, in this study, using IBM SPSS Statistics 27 statistical analysis software, we selected the multivariate linear stepwise regression method based on the correlation between the biomasses of different types of tree species and modeling factors. We retained factors with strong significance and eliminated those with weak significance until we formed the optimal model equation for estimating aboveground carbon storage for different tree species. The DBH and H of each tree extracted from the backpack LiDAR were used as independent variables (a Pearson correlation analysis showed a significant correlation between DBH and H, with $R = 0.7$, $p < 0.05$), and the measured aboveground carbon storage as the dependent variable. Various linear and nonlinear fitting models were applied using Excel to explore the relationship between forest structural variables (such as DBH and H) and predicted AGC. The best-fitting model was then selected from among these models (Tables 4 and 5).

Table 4. Multivariate stepwise linear regression modeling for LiDAR prediction of AGC in Larix.

Variable	Model	R ²	RMSE
DBH _{LiDAR}	$AGC_{LiDAR} = 0.0962 \times DBH_{LiDAR}^{2.1023}$	0.937	4.19
DBH _{LiDAR}	$AGC_{LiDAR} = 3.7302 \times DBH_{LiDAR} - 25.612$	0.882	5.94
H _{LiDAR}	$AGC_{LiDAR} = 2.9865 \times H_{LiDAR}^{1.0256}$	0.244	14.28
H _{LiDAR}	$AGC_{LiDAR} = 5.6161 \times H_{LiDAR} - 0.9979$	0.230	14.63
DBH _{LiDAR} × H _{LiDAR}	$AGC_{LiDAR} = 0.1272 (DBH_{LiDAR} \times H_{LiDAR})^{1.1291}$	0.770	11.20
DBH _{LiDAR} × H _{LiDAR}	$AGC_{LiDAR} = 0.2634 (DBH_{LiDAR} \times H_{LiDAR}) - 2.2132$	0.737	11.97
DBH _{LiDAR} + H _{LiDAR}	$AGC_{LiDAR} = 0.0124 (DBH_{LiDAR} + H_{LiDAR})^{2.4667}$	0.904	7.60
DBH _{LiDAR} + H _{LiDAR}	$AGC_{LiDAR} = 2.7801 (DBH_{LiDAR} + H_{LiDAR}) - 33.604$	0.847	11.39

Table 5. Multivariate stepwise linear regression modeling for LiDAR prediction of AGC in Betula.

Variable	Model	R ²	RMSE
DBH _{LiDAR}	$AGC_{LiDAR} = 0.1724 \times DBH_{LiDAR}^{1.9684}$	0.948	3.71
DBH _{LiDAR}	$AGC_{LiDAR} = 4.4728 \times DBH_{LiDAR} - 28.31$	0.939	4.56
H _{LiDAR}	$AGC_{LiDAR} = 0.0391 \times H_{LiDAR}^{2.534}$	0.411	17.26
H _{LiDAR}	$AGC_{LiDAR} = 5.3764 \times H_{LiDAR} - 39.113$	0.281	17.00
DBH _{LiDAR} × H _{LiDAR}	$AGC_{LiDAR} = 0.0151 (DBH_{LiDAR} \times H_{LiDAR})^{1.4633}$	0.942	5.74
DBH _{LiDAR} × H _{LiDAR}	$AGC_{LiDAR} = 0.2659 (DBH_{LiDAR} \times H_{LiDAR}) - 15.195$	0.909	6.65
DBH _{LiDAR} + H _{LiDAR}	$AGC_{LiDAR} = 0.002 (DBH_{LiDAR} + H_{LiDAR})^{2.9239}$	0.938	5.47
DBH _{LiDAR} + H _{LiDAR}	$AGC_{LiDAR} = 3.3565 (DBH_{LiDAR} + H_{LiDAR}) - 56.464$	0.880	7.41

In this study, simple stepwise regression fitting methods were used to establish various linear and nonlinear models that relate LiDAR-estimated forest structural variables such as tree height (H) and diameter at breast height (DBH) with the measured forest AGC. The model with the highest correlation coefficient was selected from multiple fitted models. As shown in Tables 4 and 5, among all the trained multivariate linear and nonlinear models, the multivariate power model exhibited higher accuracy than the multivariate linear model. In *L. gmelinii* forests, the LiDAR-estimated DBH provided the best fit for predicting *L. gmelinii* AGC ($R^2 = 0.9371$). Similarly, in *B. platyphylla* forests, the LiDAR-estimated DBH was the best predictor for *B. platyphylla* AGC ($R^2 = 0.9482$). Therefore, in this study, a power function regression model was used, with LiDAR-estimated DBH as the predictor, to simulate and predict AGC in *L. gmelinii* and *B. platyphylla* forests, respectively. The optimal prediction regression models are shown in Equations (10) and (11):

$$AGC_{Larix_LiDAR} = 0.0962 \times DBH_{LiDAR}^{2.1023} \quad (10)$$

$$AGC_{Betula_LiDAR} = 0.1724 \times DBH_{LiDAR}^{1.9684} \quad (11)$$

Using the aforementioned formulas, the AGC of *L. gmelinii* and *B. platyphylla* forests was predicted using LiDAR data. Figure 9 shows the results of the accuracy validation of

the AGC predicted by the LiDAR MSLR model compared with the AGC estimated in the field in *L. gmelinii* and *B. platyphylla* forests. As demonstrated, the AGC of *L. gmelinii* and *B. platyphylla* predicted by LiDAR using the MSLR model was significantly correlated with the measured AGC, with R^2 values of 0.91 and 0.94, RMSE values of 6.21 and 5.20, RRMSE values of 19.36% and 18.37%, and MAE values of 3.83 and 3.32, respectively. Among the two different tree species, the R^2 , RMSE, RRMSE, and MAE values were greatest for the *B. platyphylla* forests.

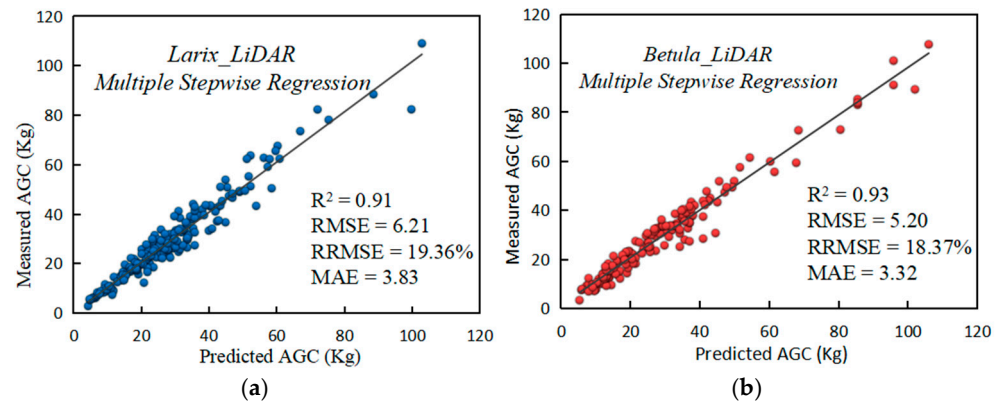


Figure 9. Forest AGC (Tg) of (a) Larix and (b) Betula measured via LiDAR using the MSLR model versus the predicted forest AGC. (Blue dots indicate data sample points for Larix; red dots indicate data sample points for Betula).

3.2.2. Aboveground Carbon Stock Estimation in Forests Based on LiDAR Remote Sensing Using the Random Forest Regression Method

In this study, 186 *L. gmelinii* trees and 164 *B. platyphylla* trees were randomly selected for RF modeling. Figure 10 shows the results of the accuracy validation of the AGC predicted by the LiDAR RF model compared with the AGC estimated in the field in *L. gmelinii* and *B. platyphylla* forests. As illustrated, the AGCs of *L. gmelinii* and *B. platyphylla* predicted by LiDAR via the RF model were significantly correlated with the measured AGC, with R^2 values of 0.9501 and 0.9618, RMSE values of 4.4023 and 3.54, RRMSE values of 13.61% and 14.03%, and MAE values of 3.2041 and 2.79, respectively. Among the two different tree species, the R^2 , RMSE, RRMSE, and MAE values were greatest for the *B. platyphylla* forests. Overall, the fitting models based on RF performed better than those based on MSLR.

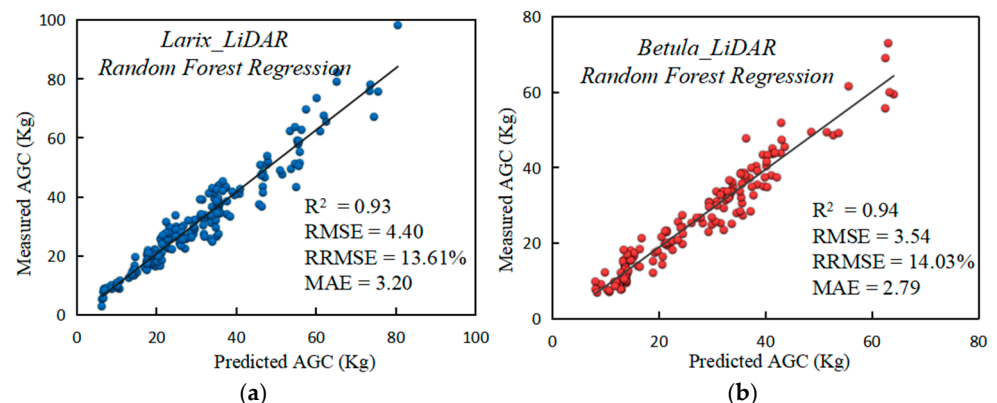


Figure 10. Forest AGC (Tg) of (a) Larix and (b) Betula measured by LiDAR using the RF model versus the predicted forest AGC. (Blue dots indicate data sample points for Larix; red dots indicate data sample points for Betula).

3.3. Estimation of Aboveground Carbon Stocks in Forests at the Sample Site Scale Based on Multisource Remote Sensing Data

3.3.1. Aboveground Carbon Stock Estimation in Forests Based on Multisource Remote Sensing Using Multiple Stepwise Linear Regression Methods

Considering the shortcomings of LiDAR data, which are spatially discrete and do not have imaging capability, multispectral information was combined to improve the accuracy of forest AGC estimation on the basis of obtaining LiDAR tree height and diameter at breast height (DBH). In this study, based on previous estimates of forest AGC using LiDAR data, the inversion model was optimized by combining multispectral imagery to complement the spectral information of vegetation. First, the UAV multispectral orthorectified image was opened, and the required individual band information (red, near-infrared, blue, green, etc.) was extracted in ArcGIS 10.7. Second, seven vegetation indices, such as the NDVI, DVI, EVI, RVI, NDRE, GNDVI, and SAVI, were calculated using the above band information, and the results of each index were saved as separate GeoTIFF files. Finally, a Pearson correlation analysis was conducted using IBM SPSS Statistics 27 software to assess the relationship between the seven vegetation indices and the measured AGC (as shown in Table 6). This analysis was used to identify the optimal vegetation indices that could enhance the accuracy of AGC estimation. As known from Table 3, the seven selected vegetation indices were weakly correlated with the measured AGC. The vegetation index with the highest correlation with forest AGC in larch forests was RVI, while the index with the highest correlation with forest AGC in birch forests was GNDVI.

Table 6. Vegetation index and measured AGC—Pearson correlation.

Vegetation Index	Correlation	
	Larix	Betula
NDVI	0.0397	0.1273
DVI	0.0417	0.1162
EVI	0.0407	0.0903
RVI	0.0426	0.1328
NDRE	0.0413	0.1329
GNDVI	0.0367	0.1614
SAVI	0.0235	0.0861

Through the analysis of the correlation between AGC and modeling factors in the sample data of larch and birch forests, we found a weak correlation between various modeling factors and AGC. We hypothesize that incorporating these vegetation indices could improve the accuracy of AGC predictions. Therefore, in this study, we combined multispectral indices with LiDAR parameters to develop models. For *L. gmelinii*, DBH and H extracted from LiDAR data, along with the vegetation index RVI calculated from UAV multispectral imagery, were used as independent variables, with the measured AGC as the dependent variable. For *B. platyphylla*, DBH, H, and the vegetation index GNDVI were used as independent variables, with the measured AGC as the dependent variable. Various linear and nonlinear fitting models were applied using Excel to explore the relationship between these forest structure variables and the predicted AGC. The best-fitting models were selected from multiple models, and predictive AGC models under multi-source remote sensing were established using various linear and nonlinear equations, with the optimal model chosen for AGC prediction (Tables 7 and 8). As indicated in the following two tables, similar to the regression models predicting AGC with LiDAR, multivariate power models exhibit higher accuracy than multivariate linear models among all the models. The use of the RVI alone for predicting AGC had poor effectiveness ($R^2 = 0.043$, RMSE = 29.02). However, incorporating LiDAR parameters such as DBH and tree height significantly improves the prediction performance and modeling accuracy. In *L. gmelinii* forests, the AGC prediction model with the highest accuracy was constructed via simple power function fitting of the RVI combined with the LiDAR DBH ($R^2 = 0.939$, RMSE = 5.06)

(Table 7). Similarly, in *B. platyphylla* forests, the highest accuracy was achieved using a simple power function fitting of the GNDVI combined with the LiDAR DBH ($R^2 = 0.942$, RMSE = 3.67) (Table 8). These results are more accurate than those of models fitted with only LiDAR data, significantly enhancing the precision of AGC fitting. This outcome reflects that while vegetation indices can provide some information about the horizontal structure of vegetation cover, they lack information on the vertical structure of vegetation height and are prone to saturation. However, incorporating LiDAR parameters not only overcomes saturation issues but also enhances the accuracy of AGC estimation.

Table 7. Multivariate stepwise linear regression modeling for multisource remote sensing prediction of AGC in Larix.

Variable	Model	R ²	RMSE
RVI	$AGC_{RVI} = 13.802 \times RVI - 12.697$	0.043	29.02
$RVI + H_{LiDAR}$	$AGC_{RVI+H(LiDAR)} = 3.5266 \times (RVI + H_{LiDAR}) - 11.54$	0.394	27.21
$RVI \times H_{LiDAR}$	$AGC_{RVI \times H(LiDAR)} = 1.0189 \times (RVI \times H_{LiDAR}) + 1.6993$	0.386	14.48
$RVI \times DBH_{LiDAR}$	$AGC_{RVI \times DBH(LiDAR)} = 1.268 \times (RVI \times DBH_{LiDAR}) - 30.04$	0.889	6.16
$RVI \times DBH_{LiDAR}$	$AGC_{RVI \times DBH(LiDAR)} = 0.0106 \times (RVI \times DBH_{LiDAR})^{2.039}$	0.924	5.74
$RVI + DBH_{LiDAR}$	$AGC_{RVI+DBH(LiDAR)} = 4.3185 \times (RVI + DBH_{LiDAR}) - 46.748$	0.913	5.37
$RVI + DBH_{LiDAR}$	$AGC_{RVI+DBH(LiDAR)} = 0.0144 (RVI + DBH_{LiDAR})^{2.6197}$	0.939	5.06
$RVI + (DBH + H)_{LiDAR}$	$AGC_{RVI+(DBH+H)_{LiDAR}} = 0.0102 [RVI + (DBH + H)_{LiDAR}]^{2.4015}$	0.863	6.80
$RVI \times (DBH + H)_{LiDAR}$	$AGC_{RVI \times (DBH+H)_{LiDAR}} = 0.006 [RVI \times (DBH + H)_{LiDAR}]^{1.9538}$	0.818	8.55
$RVI + (DBH \times H)_{LiDAR}$	$AGC_{RVI+(DBH \times H)_{LiDAR}} = 0.2316 [RVI + (DBH \times H)_{LiDAR}]^{0.9215}$	0.774	8.37
$RVI \times (DBH \times H)_{LiDAR}$	$AGC_{RVI \times (DBH \times H)_{LiDAR}} = 0.1075 [RVI \times (DBH \times H)_{LiDAR}]^{2.0231}$	0.759	8.94

Table 8. Multivariate stepwise linear regression modeling for multisource remote sensing prediction of AGC in Betula.

Variable	Model	R ²	RMSE
$GNDVI + H_{LiDAR}$	$AGC_{GNDVI+H(LiDAR)} = 3.6502 \times (GNDVI + H_{LiDAR}) - 21.84$	0.191	16.41
$GNDVI \times H_{LiDAR}$	$AGC_{GNDVI \times H(LiDAR)} = 5.9133 \times (GNDVI \times H_{LiDAR}) - 11.63$	0.150	16.82
$GNDVI \times DBH_{LiDAR}$	$AGC_{GNDVI \times DBH(LiDAR)} = 8.4868 \times (GNDVI \times DBH_{LiDAR}) - 26.025$	0.903	5.67
$GNDVI \times DBH_{LiDAR}$	$AGC_{GNDVI \times DBH(LiDAR)} = 0.7576 \times (GNDVI \times DBH_{LiDAR})^{1.9001}$	0.919	4.95
$GNDVI + DBH_{LiDAR}$	$AGC_{GNDVI+DBH(LiDAR)} = 4.4075 \times (GNDVI + DBH_{LiDAR}) - 29.202$	0.933	4.49
$GNDVI + DBH_{LiDAR}$	$AGC_{GNDVI+DBH(LiDAR)} = 0.1424 (GNDVI + DBH_{LiDAR})^{2.0231}$	0.942	3.67
$GNDVI + (DBH + H)_{LiDAR}$	$AGC_{GNDVI+(DBH+H)_{LiDAR}} = 0.0017 [GNDVI + (DBH + H)_{LiDAR}]^{2.9292}$	0.911	5.32
$GNDVI \times (DBH + H)_{LiDAR}$	$AGC_{GNDVI \times (DBH+H)_{LiDAR}} = 0.0248 [GNDVI \times (DBH + H)_{LiDAR}]^{2.6788}$	0.845	0.76
$GNDVI + (DBH \times H)_{LiDAR}$	$AGC_{GNDVI+(DBH \times H)_{LiDAR}} = 0.0166 [GNDVI + (DBH \times H)_{LiDAR}]^{1.4349}$	0.923	5.84
$GNDVI \times (DBH \times H)_{LiDAR}$	$AGC_{GNDVI \times (DBH \times H)_{LiDAR}} = 0.0495 [GNDVI \times (DBH \times H)_{LiDAR}]^{1.4068}$	0.905	6.80

This study employs a combination of the multispectral vegetation indices RVI and GNDVI with LiDAR data for modeling, constructs models using various linear and nonlinear equations, and selects the best models for predicting forest AGCs. In *L. gmelinii* forests, the combination of multisource remote sensing-estimated DBH + RVI (power function) yielded the best fit for predicting AGCs, with an R^2 value of 0.939. In *B. platyphylla* forests, the combination of DBH + GNDVI (power function) estimated through multisource remote sensing provides the best fit for predicting AGCs, with an R^2 value of 0.942.

$$AGC_{Larix_LiDAR\delta multispectral} = 0.0144 \times (DBH_{LiDAR} + RVI_{multispectral})^{2.6197} \quad (12)$$

$$AGC_{Betula_LiDAR\delta multispectral} = 0.1424 \times (DBH_{LiDAR} + GNDVI_{multispectral})^{2.0231} \quad (13)$$

Using Equations (12) and (13), the AGC of *L. gmelinii* and *B. platyphylla* forests is predicted through multisource remote sensing. Figure 11 shows the results of the accuracy validation of the AGC predicted by the multisource remote sensing MSLR model compared with the AGC estimated in the field in *L. gmelinii* and *B. platyphylla* forests. As demonstrated,

the AGC of *L. gmelinii* and *B. platyphylla* predicted by multisource remote sensing using the MSLR model was significantly correlated with the measured AGC, with R^2 values of 0.92 and 0.96, RMSE values of 6.15 and 3.57, RRMSE values of 19.06% and 12.44%, and MAE values of 4.41 and 2.70, respectively. Among the two different tree species, the R^2 , RMSE, RRMSE, and MAE values were greatest for *B. platyphylla* forests. Compared to the AGC predicted solely with LiDAR, the accuracy improved by 0.01 and 0.03, respectively.

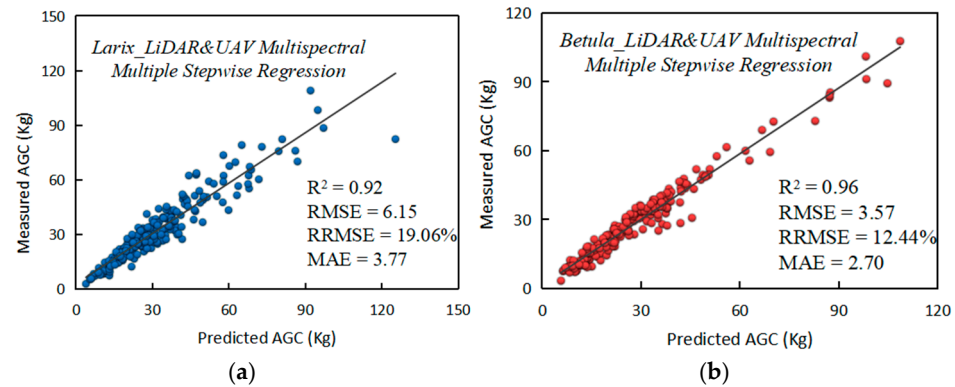


Figure 11. Forest AGC (Tg) of (a) Larix and (b) Betula measured by multisource remote sensing using the MSLR model versus the predicted forest AGC. (Blue dots indicate data sample points for Larix; red dots indicate data sample points for Betula).

3.3.2. Aboveground Carbon Stock Estimation in Forests Based on Multisource Remote Sensing Using a Random Forest Regression Approach

Figure 12 shows the results of the accuracy validation of the AGC predicted by the multisource remote sensing RF model compared with the AGC estimated in the field in *L. gmelinii* and *B. platyphylla* forests. The results indicate a significant correlation between the predicted AGC via multisource remote sensing via the RF model and the measured AGC for both tree species. The R^2 values for *L. gmelinii* and *B. platyphylla* were both 0.95, the RMSE values were 3.99 and 3.45, the RRMSE values were 12.49% and 13.83%, and the MAE values were 3.10 and 2.78. Among these two different tree species, the R^2 , RMSE, RRMSE, and MAE values were greatest in *B. platyphylla* forests. Moreover, compared to the AGC predicted solely with LiDAR, there was an improvement in accuracy of 0.02 for *L. gmelinii* and 0.01 for *B. platyphylla*.

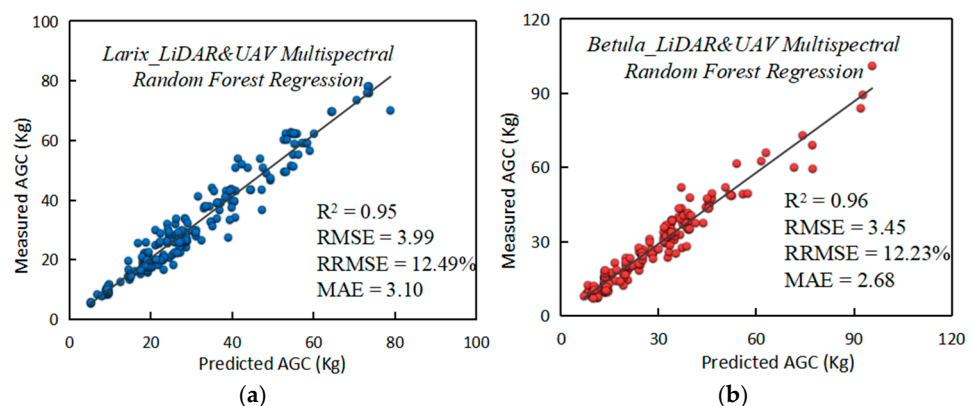


Figure 12. Forest AGC (Tg) of (a) Larix and (b) Betula measured by multisource remote sensing using the RF model versus the predicted forest AGC. (Blue dots indicate data sample points for Larix; red dots indicate data sample points for Betula).

3.4. Comparative Analysis of Multiple Stepwise Linear Regression and Random Forest Regression Models Based on Different Remote Sensing Methods

This study utilized various remote sensing data and employed both MSLR and RF regression models to predict the AGC of *L. gmelinii* and *B. platyphylla* forests. Figures 13 and 14 display comparisons between the prediction results of these two models under the different remote sensing data and the actual observation results for AGC. Overall, the R^2 values show an increasing trend from left to right, approaching 1, indicating progressively better model fitting. The RMSE, RRMSE, and MAE values display a decreasing trend from left to right, suggesting that the smaller these values are, the less the discrepancy between the model predictions and observed values, and the better the predictive power of the model. This overall trend indicates the feasibility of the models. Specifically: (1) Among both the parametric and nonparametric models, the RF model constructed from machine learning algorithms demonstrated greater accuracy in estimating AGC for *L. gmelinii* and *B. platyphylla* forests than the MSLR model. (2) When combining vegetation indices from UAV multispectral images with LiDAR remote sensing data in the MSLR and RF models for estimating forest AGC, the accuracy surpasses that of using only LiDAR remote sensing data. (3) In both *L. gmelinii* and *B. platyphylla* forests, regardless of whether the MSLR or RF model was used, the accuracy of estimating forest AGC was greater for *B. platyphylla* than for *L. gmelinii*.

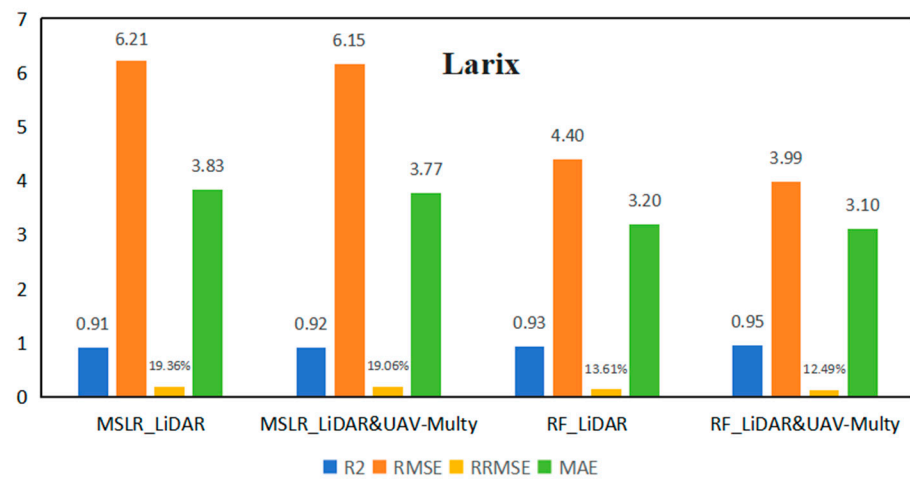


Figure 13. Comparison of the prediction results of two models based on different remote sensing data on the AGC of Larix with the actual observation results.

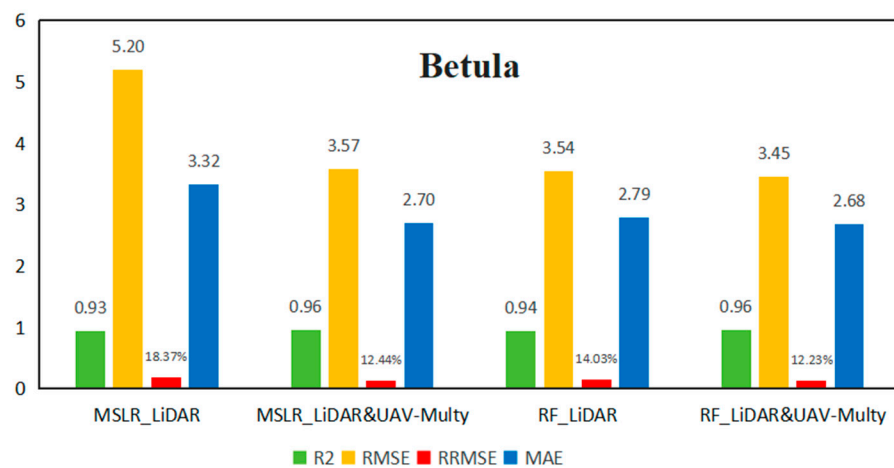


Figure 14. Comparison of the prediction results of two models based on different remote sensing data on the AGC of Betula with the actual observation results.

4. Discussion

4.1. Potential of LiDAR Combined with Multispectral Imagery for Estimating AGC in Forests

Compared to manual measurements, backpack LiDAR offers precise scanning and real-time data integration while in motion, providing a more flexible and efficient method for forest inventory collection [60]. In the data collection process, backpack LiDAR requires only one surveyor to carry the equipment across the measurement site, significantly reducing time and costs and improving efficiency [61]. As shown in Table 9, when collecting point cloud data for a 10 m × 40 m sample, traditional measurement methods require 3–4 people to complete the data collection, whereas backpack LiDAR needs only one person. While traditional manual measurements take approximately 36 min to measure a plot, backpack LiDAR takes only approximately 5 min. Preprocessing the collected data via traditional methods took approximately 14 min, while preprocessing the backpack LiDAR point cloud data took approximately 10 min. The internal data processing time depends on the size of the dataset and the computer configuration. Overall, compared with traditional methods, backpack LiDAR saves approximately 30 min per plot, illustrating its time efficiency. In terms of optical data, acquiring airborne multispectral images under favorable weather conditions enhances efficiency and reduces costs to a certain extent. Therefore, the combined use of optical imagery and LiDAR further reduces the cost of assessing forest emission reductions. This combination enables the mapping of large areas near real-time carbon stocks [62]. The findings of this study underscore the high precision and potential of LiDAR technology for estimating AGC, offering significant value for enhancing forest management practices and informing sustainable ecosystem management strategies [63]. However, scaling up this approach to a broader level may present significant challenges, particularly in low-income countries where limited financial and technical resources could hinder its widespread implementation and reduce its overall effectiveness [64].

Table 9. Timing comparison between traditional and Backpack LiDAR measurement methods.

Measurement Method	Personnel	Sample Site (m ²)	Time Consumption (min)		
			Data Collection	Data Processing	Total
Traditional measurement	3–4	10 × 40	30:16	14:16	44:32
Backpack LiDAR	1	10 × 40	5:42	10:04	15:46

Optical images have been applied in earlier studies to estimate forest AGB and AGCs, but the results showed that optical signals are weakly penetrating. Spectral images mainly record the horizontal structure of the forest and cannot record the vertical structure information of the forest. However, LiDAR can penetrate the forest canopy and record vertical structure information. This approach compensates for the shortcomings of optical images. In this study, there are two main reasons for the small improvement after adding multispectral information. The first reason may be that when the visible light of multispectral data is saturated in dense forest areas [65], the accuracy is lower in complex forest structures, resulting in the deviation of the AGC estimated by the NDVI from the measured AGC. Another reason for this difference may be that the LiDAR forest structure attributes themselves have a strong correlation with AGC, and the addition of multispectral information did not result in much improvement. Overall, although these improvements are not significant, novel multisensor earth observation methods that involve the combination of satellite-borne LiDAR data with optical data using machine learning techniques enable accurate measurements of carbon stocks and provide effective data support for forest emission reduction. For example, Jiao et al. [66] proposed a practical framework for assessing forest emission reductions via the fusion of optical satellite imagery and spaceborne LiDAR data. Shen et al. mapped subtropical forest AGB data by combining Landsat TM/ETM+ and ALOS 1-band SAR imagery from Guangdong Province, and the results demonstrated that multisensor imagery-based AGBs had a good correlation [67,68].

Our results further suggest that combining LiDAR and multispectral data is essential for improving the accuracy of AGB and AGC estimation.

4.2. Main Challenges and Uncertainty Analyses for Estimating Forest AGCs

In response to the challenges in estimating vegetation biomass and carbon storage (specifically, whether obtaining large-scale forest structure and spectral information improves biomass and carbon stock estimations [69]), this study integrates forest structural attributes and spectral data to estimate forest AGCs at the plot level. Despite the difficulty in accurately capturing AGC changes in forests with complex structures using only structural and spectral information, the heterogeneity of canopy spectral information provided by multispectral images has enhanced the accuracy of our multisource data integration modeling approach, increasing the AGC estimation accuracy from 90.29% to 90.6%. Additionally, we utilized various multiple linear regression and power regression models to select the best-fitting models for AGC estimation. Compared to multiple linear regression models, power regression models exhibited greater accuracy in AGC estimation. This indicates that the dominant tree species in our study area, *L. gmelinii*, conforms to a power allometric relationship and that using this relationship can improve the accuracy of forest AGC estimates. Therefore, the power allometric relationship based on forest structural attributes and spectral information represents a new method for enhancing AGC estimation. This method can be used to explore the relationship between tree metabolism and biomass [70], and such relationships may be more stable in similar landscapes [71].

However, there are still uncertainties in this study. First, the laser beams of backpack LiDAR cannot penetrate the lower canopy layers in dense forest structures; second, due to obstruction from the understory, backpack LiDAR faces challenges in capturing the treetops of the upper canopy, resulting in notable differences between the LiDAR-estimated and actual measured heights. The results and conclusions of this study are currently valid only for coniferous forests with relatively simple stand structures, and further validation is needed for broadleaf forests, mixed forests, or other forest types with more complex structures based on additional forest plots and remote sensing data. In addition, this study utilized ultra-high-resolution UAV imagery with a spatial resolution of 0.02 m. While such high spatial detail enables capturing fine-scale variations, it may also introduce significant spatial variability, particularly in areas with heterogeneous vegetation distribution. This level of granularity can result in weak correlations between vegetation indices (VI) and AGC, ultimately impacting the model's predictive accuracy. Despite the observed low correlation in our findings, VI still holds considerable promise for capturing ecosystem dynamics and monitoring environmental changes [72].

4.3. Research and Perspectives on Estimating Late-Season Forest AGCs

This study revolves around the theme of estimating regional-scale forest AGCs by integrating multispectral imagery and LiDAR data; encompassing a comprehensive and systematic exploration from field data collection to preprocessing steps such as atmospheric, radiometric, and geometric correction of multispectral imagery and cropping; resampling, denoising, filtering, ground classification, and normalization of LiDAR data; constructing forest AGC estimation models suitable for complex terrain conditions; and then spatially extrapolating regional-scale forest AGCs. However, due to the scarcity of field measurement data and the complexity of mountainous terrain, the accuracy of regional forest AGC estimation combined with multisource remote sensing data is still not precise enough, warranting further research.

At the current stage, calibration and validation still require high-quality field measurement data. Due to the complex terrain of mountainous areas, more accessible sites were chosen for field inventory collection, resulting in spatial discontinuity and discreteness in the regional forest AGC density spatial distribution map. Future research should aim to select spatially continuous plots for data collection. Limited by time, the collected samples

were insufficient, suitable only for single-tree or regional forest AGC estimation, and not representative of the entire forest AGC storage in the Dulaer forest.

The backpack LiDAR data collection is affected by poor GPS signals, directly impacting the quality of trajectory files and leading to failures in point cloud resolution or significant errors in absolute coordinates. Moreover, obtaining high-precision absolute coordinate point cloud data is crucial for determining individual tree locations within sample areas. Therefore, efficiently and accurately collecting absolute geographical reference point cloud data in dense forests without GPS signals will be a focus of future research. Additionally, in *L. gmelinii* plots with dense branches, it was necessary to cut branches in advance along the designed route to ensure the safe operation of the backpack LiDAR, which affects the data collection time and quality. Thus, the accuracy of image data collection via backpack LiDAR needs further verification in more operational environments. The multispectral data used in this study had limited spectral bands, resulting in less correlation between the calculated vegetation spectral indices and forest AGC. Future research should explore the capability of regional forest spectral inversion via hyperspectral imaging via UAVs at different flight altitudes in conjunction with LiDAR data. To further mitigate the impact of spatial variability, future research could explore the use of Object-Based Image Analysis (OBIA) and texture features. These advanced methodologies offer more stable and structured variables by grouping adjacent pixels into cohesive objects based on their spectral and morphological similarities, thereby minimizing the variability inherent in high-resolution data. Additionally, texture features can capture the intricate spatial patterns and distribution characteristics of vegetation, providing a richer representation of the landscape and ultimately enhancing the precision of AGC estimation [71,72].

In summary, combining LiDAR data with traditional remote sensing data can complement data sources better, facilitating the acquisition and classification of ground information and improving the accuracy of ecological parameter estimation, ecological monitoring, and simulation. Effectively integrating multisource remote sensing data for ecological research is currently a trending topic.

5. Conclusions

In this study, LiDAR and multispectral data were effectively integrated to estimate the AGC of Xing'an larch and white birch forests. The findings highlight the strong correlation between LiDAR-derived forest structure attributes and the AGC, underscoring the critical role of LiDAR in carbon monitoring and assessment. Although the relationship between vegetation indices (VI) and the AGC was comparatively weaker, their potential value in ecological monitoring and assessment should not be overlooked and warrants further investigation. This research serves as a valuable reference for future applications of multi-source remote sensing technologies in forest carbon stock estimation, particularly in assessing their feasibility and effectiveness under diverse environmental conditions.

Author Contributions: R.S.: Data curation, Formal analysis, Writing—original draft, Writing—review & editing author; W.D.: Methodology, Project administration, Supervision, Writing—review & editing author; H.Y.: Investigation, Supervision; Y.S.: Conceptualization; Funding acquisition author; W.R.: Resources, Supervision; R.L.: Software, Validation. All authors have read and agreed to the published version of the manuscript.

Funding: This research was supported by several key funding initiatives, including the Science and Technology Programme of Inner Mongolia Autonomous Region (2024KJHZ0002 and 2022YFSH0027), the Key Special Project of Inner Mongolia's "Science and Technology for the Development of Mongolia" Action Plan (2020ZD0028), and the Project for Introducing High-Level Talents of Inner Mongolia Autonomous Region (2022NMRC003). Additional support was provided by the National Natural Science Foundation of China (42201374), the Natural Science Foundation of Inner Mongolia Autonomous Region (2022LHQN04001), and the "Integrated Demonstration of Ecological Protection and Comprehensive Utilization of Resource Technology in Aershan" under the Central Guidance of Local Science and Technology Development Funds. We also acknowledge the "Introduction of

High-Level Talents Project” and the Master’s Degree Research and Innovation Fund (CXJJS23065) of Inner Mongolia Normal University (2020YJRC050).

Data Availability Statement: The original contributions presented in the study are included in the article, further inquiries can be directed to the corresponding author.

Acknowledgments: We are grateful for the fieldwork support from the Inner Mongolia Key Laboratory of Remote Sensing and Geographic Information Systems and for the support of the Arshan Forest and Grassland Disaster Prevention and Mitigation Field Scientific Observation and Research Station of the Inner Mongolia Autonomous Region.

Conflicts of Interest: The authors declare no conflict of interest.

References

1. Wani, A.A.; Joshi, P.K.; Singh, O. Estimating Biomass and Carbon Mitigation of Temperate Coniferous Forests Using Spectral Modeling and Field Inventory Data. *Ecol. Inform.* **2015**, *25*, 63–70. [[CrossRef](#)]
2. Su, R.; Du, W.; Ying, H.; Shan, Y.; Liu, Y. Estimation of Aboveground Carbon Stocks in Forests Based on LiDAR and Multispectral Images: A Case Study of Duraer Coniferous Forests. *Forests* **2023**, *14*, 992. [[CrossRef](#)]
3. Luderer, G.; Vrontisi, Z.; Bertram, C.; Edelenbosch, O.Y.; Pietzcker, R.C.; Rogelj, J.; De Boer, H.S.; Drouet, L.; Emmerling, J.; Fricko, O.; et al. Residual Fossil CO₂ Emissions in 1.5–2 °C Pathways. *Nat. Clim. Chang.* **2018**, *8*, 626–633. [[CrossRef](#)]
4. Poorazimy, M.; Shataee, S.; McRoberts, R.E.; Mohammadi, J. Integrating Airborne Laser Scanning Data, Space-Borne Radar Data and Digital Aerial Imagery to Estimate Aboveground Carbon Stock in Hyrcanian Forests, Iran. *Remote Sens. Environ.* **2020**, *240*, 111669. [[CrossRef](#)]
5. Chen, Y.; Li, L.; Lu, D.; Li, D. Exploring Bamboo Forest Aboveground Biomass Estimation Using Sentinel-2 Data. *Remote Sens.* **2018**, *11*, 7. [[CrossRef](#)]
6. Nandy, S.; Srinet, R.; Padalia, H. Mapping Forest Height and Aboveground Biomass by Integrating ICESat-2, Sentinel-1 and Sentinel-2 Data Using Random Forest Algorithm in Northwest Himalayan Foothills of India. *Geophys. Res. Lett.* **2021**, *48*, e2021GL093799. [[CrossRef](#)]
7. Li, W.; Niu, Z.; Shang, R.; Qin, Y.; Wang, L.; Chen, H. High-Resolution Mapping of Forest Canopy Height Using Machine Learning by Coupling ICESat-2 LiDAR with Sentinel-1, Sentinel-2 and Landsat-8 Data. *Int. J. Appl. Earth Obs. Geoinf.* **2020**, *92*, 102163. [[CrossRef](#)]
8. Li, M.; Im, J.; Quackenbush, L.J.; Liu, T. Forest Biomass and Carbon Stock Quantification Using Airborne LiDAR Data: A Case Study Over Huntington Wildlife Forest in the Adirondack Park. *IEEE J. Sel. Top. Appl. Earth Obs. Remote Sens.* **2014**, *7*, 3143–3156. [[CrossRef](#)]
9. Luo, S.; Wang, C.; Xi, X.; Pan, F.; Peng, D.; Zou, J.; Nie, S.; Qin, H. Fusion of Airborne LiDAR Data and Hyperspectral Imagery for Aboveground and Belowground Forest Biomass Estimation. *Ecol. Indic.* **2017**, *73*, 378–387. [[CrossRef](#)]
10. Chen, Q.; McRoberts, R. Statewide Mapping and Estimation of Vegetation Aboveground Biomass Using Airborne Lidar. In Proceedings of the 2016 IEEE International Geoscience and Remote Sensing Symposium (IGARSS), Beijing, China, 10–15 July 2016; IEEE: Beijing, China, 2016; pp. 4442–4444.
11. Tao, S.; Wu, F.; Guo, Q.; Wang, Y.; Li, W.; Xue, B.; Hu, X.; Li, P.; Tian, D.; Li, C.; et al. Segmenting Tree Crowns from Terrestrial and Mobile LiDAR Data by Exploring Ecological Theories. *ISPRS J. Photogramm. Remote Sens.* **2015**, *110*, 66–76. [[CrossRef](#)]
12. Holmgren, J.; Tulldahl, H.M.; Nordlöf, J.; Nyström, M.; Olofsson, K.; Rydell, J.; Willén, E. Estimation of tree position and stem diameter using simultaneous localization and mapping with data from a backpack-mounted laser scanner. *Int. Arch. Photogramm. Remote Sens. Spat. Inf. Sci.* **2017**, *XLII-3/W3*, 59–63. [[CrossRef](#)]
13. Oveland, I.; Hauglin, M.; Giannetti, F.; Schipper Kjorsvik, N.; Gobakken, T. Comparing Three Different Ground Based Laser Scanning Methods for Tree Stem Detection. *Remote Sens.* **2018**, *10*, 538. [[CrossRef](#)]
14. Su, Y.; Guo, Q.; Fry, D.L.; Collins, B.M.; Kelly, M.; Flanagan, J.P.; Battles, J.J. A Vegetation Mapping Strategy for Conifer Forests by Combining Airborne LiDAR Data and Aerial Imagery. *Can. J. Remote Sens.* **2016**, *42*, 1–15. [[CrossRef](#)]
15. Cutler, M.E.J.; Boyd, D.S.; Foody, G.M.; Vetrivel, A. Estimating Tropical Forest Biomass with a Combination of SAR Image Texture and Landsat TM Data: An Assessment of Predictions between Regions. *ISPRS J. Photogramm. Remote Sens.* **2012**, *70*, 66–77. [[CrossRef](#)]
16. Nichol, J.E.; Sarker, M.d.L.R. Improved Biomass Estimation Using the Texture Parameters of Two High-Resolution Optical Sensors. *IEEE Trans. Geosci. Remote Sens.* **2011**, *49*, 930–948. [[CrossRef](#)]
17. Reddersen, B.; Fricke, T.; Wachendorf, M. A Multi-Sensor Approach for Predicting Biomass of Extensively Managed Grassland. *Comput. Electron. Agric.* **2014**, *109*, 247–260. [[CrossRef](#)]
18. Tilly, N.; Aasen, H.; Bareth, G. Fusion of Plant Height and Vegetation Indices for the Estimation of Barley Biomass. *Remote Sens.* **2015**, *7*, 11449–11480. [[CrossRef](#)]
19. Ghosh, S.M.; Behera, M.D. Aboveground Biomass Estimation Using Multi-Sensor Data Synergy and Machine Learning Algorithms in a Dense Tropical Forest. *Appl. Geogr.* **2018**, *96*, 29–40. [[CrossRef](#)]

20. Verrelst, J.; Rivera, J.P.; Veroustraete, F.; Muñoz-Mari, J.; Clevers, J.G.P.W.; Camps-Valls, G.; Moreno, J. Experimental Sentinel-2 LAI Estimation Using Parametric, Non-Parametric and Physical Retrieval Methods—A Comparison. *ISPRS J. Photogramm. Remote Sens.* **2015**, *108*, 260–272. [[CrossRef](#)]
21. Silva, C.; Hudak, A.; Vierling, L.; Klauber, C.; Garcia, M.; Ferraz, A.; Keller, M.; Eitel, J.; Saatchi, S. Impacts of Airborne Lidar Pulse Density on Estimating Biomass Stocks and Changes in a Selectively Logged Tropical Forest. *Remote Sens.* **2017**, *9*, 1068. [[CrossRef](#)]
22. Brown, S.; Narine, L.L.; Gilbert, J. Using Airborne Lidar, Multispectral Imagery, and Field Inventory Data to Estimate Basal Area, Volume, and Aboveground Biomass in Heterogeneous Mixed Species Forests: A Case Study in Southern Alabama. *Remote Sens.* **2022**, *14*, 2708. [[CrossRef](#)]
23. Kim, S.-R.; Kwak, D.-A.; Lee, W.-K.; Son, Y.; Bae, S.-W.; Kim, C.; Yoo, S. Estimation of Carbon Storage Based on Individual Tree Detection in Pinus Densiflora Stands Using a Fusion of Aerial Photography and LiDAR Data. *Sci. China Life Sci.* **2010**, *53*, 885–897. [[CrossRef](#)] [[PubMed](#)]
24. Guisan, A.; Edwards, T.C.; Hastie, T. Generalized Linear and Generalized Additive Models in Studies of Species Distributions: Setting the Scene. *Ecol. Model.* **2002**, *157*, 89–100. [[CrossRef](#)]
25. Ahmadi, K.; Kalantar, B.; Saeidi, V.; Harandi, E.K.G.; Janizadeh, S.; Ueda, N. Comparison of Machine Learning Methods for Mapping the Stand Characteristics of Temperate Forests Using Multi-Spectral Sentinel-2 Data. *Remote Sens.* **2020**, *12*, 3019. [[CrossRef](#)]
26. Ali, I.; Greifeneder, F.; Stamenkovic, J.; Neumann, M.; Notarnicola, C. Review of Machine Learning Approaches for Biomass and Soil Moisture Retrievals from Remote Sensing Data. *Remote Sens.* **2015**, *7*, 16398–16421. [[CrossRef](#)]
27. Mu, C.; Lu, H.; Wang, B.; Cui, W. Short-Term Effects of Harvesting on Carbon Storage of Boreal Larix Gmelinii–Carex Schmidtii Forested Wetlands in Daxing’anling, Northeast China. *For. Ecol. Manag.* **2013**, *293*, 140–148. [[CrossRef](#)]
28. Liu, Y. Carbon Density in Boreal Forests Responds Non-Linearly to Temperature: An Example from the Greater Khingan Mountains, Northeast China. *Agric. For. Meteorol.* **2023**, *338*, 109519. [[CrossRef](#)]
29. Xu, Y. Current Situation of Forest Resources and Management Countermeasures in Dural Forest. Master’s Thesis, Inner Mongolia Agricultural University, Hohhot, China, 2022.
30. Fang, C.L.; Chen, Q.; Ren, Y.; Wang, Y.J. Modelling of subtropical forest biomass estimation based on airborne LiDAR. *For. Surv. Plan.* **2021**, *46*, 1–8.
31. Yang, H.; Hu, C.M.; Zhang, L.M.; Li, S.K. Progress in characterising forest carbon sinks in Inner Mongolia. *J. Appl. Ecol.* **2014**, *25*, 3366–3372. [[CrossRef](#)]
32. Daniel, I.; Rollet, B. Phytomasse Aérienne et Production Primaire Dans La Mangrove Du Grand Cul-De-Sac Marin (Guadeloupe, Antilles Françaises). *Bull. Ecol.* **1989**, *20*, 27–39.
33. Fromard, F.; Puig, H.; Mougin, E.; Marty, G.; Betoulle, J.L.; Cadamuro, L. Structure, above-Ground Biomass and Dynamics of Mangrove Ecosystems: New Data from French Guiana. *Oecologia* **1998**, *115*, 39–53. [[CrossRef](#)] [[PubMed](#)]
34. Han, A. Forest Biomass and Carbon Stock Remote Sensing Methods. Ph.D. Thesis, Beijing Forestry University, Beijing, China, 2009.
35. He, H. Carbon Sink Capacity of Xing’an Larch Primary Forest and Post-Harvest Restoration Stand. Master’s Thesis, Inner Mongolia Agricultural University, Hohhot, China, 2009.
36. Ma, Z.; Wang, S.; Wang, C.; Zhao, B.; Zhao, J.; Wu, F. A study on carbon layer delineation of natural Xing’an larch and birch forests in the DaXing’an Mountains. *J. Cent. South For. Univ. Sci. Technol.* **2017**, *37*, 112–117. [[CrossRef](#)]
37. Paustian, K.; Ravindranath, N.H.; Amstel, A.V. 2006 IPCC Guidelines for National Greenhouse Gas Inventories. *Int. Panel Clim. Chang.* **2006**, *2*, 335–346. [[CrossRef](#)]
38. Lu, D.; Chen, Q.; Wang, G.; Liu, L.; Li, G.; Moran, E. A Survey of Remote Sensing-Based Aboveground Biomass Estimation Methods in Forest Ecosystems. *Int. J. Digit. Earth* **2016**, *9*, 63–105. [[CrossRef](#)]
39. Gleason, C.J.; Im, J. A Review of Remote Sensing of Forest Biomass and Biofuel: Options for Small-Area Applications. *GIScience Remote Sens.* **2011**, *48*, 141–170. [[CrossRef](#)]
40. Jiang, F.; Deng, M.; Tang, J.; Fu, L.; Sun, H. Integrating Spaceborne LiDAR and Sentinel-2 Images to Estimate Forest Aboveground Biomass in Northern China. *Carbon Balance Manag.* **2022**, *17*, 12. [[CrossRef](#)]
41. Bannari, A.; Morin, D.; Bonn, F.; Huete, A.R. A Review of Vegetation Indices. *Remote Sens. Rev.* **1995**, *13*, 95–120. [[CrossRef](#)]
42. Crippen, R.E. Calculating the Vegetation Index Faster. *Remote Sens. Environ.* **1990**, *34*, 71–73. [[CrossRef](#)]
43. Huete, A.R. A Soil-Adjusted Vegetation Index (SAVI). *Remote Sens. Environ.* **1988**, *25*, 295–309. [[CrossRef](#)]
44. Jordan, C.F. Derivation of Leaf-Area Index from Quality of Light on the Forest Floor. *Ecology* **1969**, *50*, 663–666. [[CrossRef](#)]
45. Tucker, C.J. Red and Photographic Infrared Linear Combinations for Monitoring Vegetation. *Remote Sens. Environ.* **1979**, *8*, 127–150. [[CrossRef](#)]
46. Huete, A.; Didan, K.; Miura, T.; Rodriguez, E.P.; Gao, X.; Ferreira, L.G. Overview of the Radiometric and Biophysical Performance of the MODIS Vegetation Indices. *Remote Sens. Environ.* **2002**, *83*, 195–213. [[CrossRef](#)]
47. Buschmann, C.; Nagel, E. In Vivo Spectroscopy and Internal Optics of Leaves as Basis for Remote Sensing of Vegetation. *Int. J. Remote Sens.* **1993**, *14*, 711–722. [[CrossRef](#)]
48. Li, X.; Xiang, F.; Wu, S.; Liu, X.; Tian, Y.; Zhu, Y.; Cao, Q. A diagnostic method for nitrogen nutrition in winter wheat based on the time-series dynamics of vegetation index. *J. Wheat Crop.* **2022**, *42*, 109–119.

49. Straub, C.; Weinacker, H.; Koch, B. A Comparison of Different Methods for Forest Resource Estimation Using Information from Airborne Laser Scanning and CIR Orthophotos. *Eur. J. For. Res* **2010**, *129*, 1069–1080. [\[CrossRef\]](#)
50. Ku, N.-W.; Popescu, S.C. A Comparison of Multiple Methods for Mapping Local-Scale Mesquite Tree Aboveground Biomass with Remotely Sensed Data. *Biomass Bioenergy* **2019**, *122*, 270–279. [\[CrossRef\]](#)
51. Kronseider, K.; Ballhorn, U.; Böhm, V.; Siegert, F. Above Ground Biomass Estimation across Forest Types at Different Degradation Levels in Central Kalimantan Using LiDAR Data. *Int. J. Appl. Earth Obs. Geoinf.* **2012**, *18*, 37–48. [\[CrossRef\]](#)
52. Morin, D.; Planells, M.; Guyon, D.; Villard, L.; Mermoz, S.; Bouvet, A.; Thevenon, H.; Dejoux, J.-F.; Le Toan, T.; Dedieu, G. Estimation and Mapping of Forest Structure Parameters from Open Access Satellite Images: Development of a Generic Method with a Study Case on Coniferous Plantation. *Remote Sens.* **2019**, *11*, 1275. [\[CrossRef\]](#)
53. Fassnacht, F.E.; Hartig, F.; Latifi, H.; Berger, C.; Hernández, J.; Corvalán, P.; Koch, B. Importance of Sample Size, Data Type and Prediction Method for Remote Sensing-Based Estimations of Aboveground Forest Biomass. *Remote Sens. Environ.* **2014**, *154*, 102–114. [\[CrossRef\]](#)
54. Hudak, A.T.; Strand, E.K.; Vierling, L.A.; Byrne, J.C.; Eitel, J.U.H.; Martinuzzi, S.; Falkowski, M.J. Quantifying Aboveground Forest Carbon Pools and Fluxes from Repeat LiDAR Surveys. *Remote Sens. Environ.* **2012**, *123*, 25–40. [\[CrossRef\]](#)
55. Tanase, M.A.; Panciera, R.; Lowell, K.; Tian, S.; Hacker, J.M.; Walker, J.P. Airborne Multi-Temporal L-Band Polarimetric SAR Data for Biomass Estimation in Semi-Arid Forests. *Remote Sens. Environ.* **2014**, *145*, 93–104. [\[CrossRef\]](#)
56. Karlson, M.; Ostwald, M.; Reese, H.; Sanou, J.; Tankoano, B.; Mattsson, E. Mapping Tree Canopy Cover and Aboveground Biomass in Sudano-Sahelian Woodlands Using Landsat 8 and Random Forest. *Remote Sens.* **2015**, *7*, 10017–10041. [\[CrossRef\]](#)
57. Breiman, L. Random Forests. *Mach. Learn.* **2001**, *45*, 5–32. [\[CrossRef\]](#)
58. Adam, E.; Mutanga, O.; Abdel-Rahman, E.M.; Ismail, R. Estimating Standing Biomass in Papyrus (*Cyperus papyrus* L.) Swamp: Exploratory of in Situ Hyperspectral Indices and Random Forest Regression. *Int. J. Remote Sens.* **2014**, *35*, 693–714. [\[CrossRef\]](#)
59. Powell, S.L.; Cohen, W.B.; Healey, S.P.; Kennedy, R.E.; Moisen, G.G.; Pierce, K.B.; Ohmann, J.L. Quantification of Live Aboveground Forest Biomass Dynamics with Landsat Time-Series and Field Inventory Data: A Comparison of Empirical Modeling Approaches. *Remote Sens. Environ.* **2010**, *114*, 1053–1068. [\[CrossRef\]](#)
60. Hyypä, E.; Yu, X.; Kaartinen, H.; Hakala, T.; Kukko, A.; Vastaranta, M.; Hyypä, J. Comparison of Backpack, Handheld, Under-Canopy UAV, and Above-Canopy UAV Laser Scanning for Field Reference Data Collection in Boreal Forests. *Remote Sens.* **2020**, *12*, 3327. [\[CrossRef\]](#)
61. Ruhan, A.; Du, W.; Ying, H.; Wei, B.; Shan, Y.; Dai, H. Estimation of Aboveground Biomass of Individual Trees by Backpack LiDAR Based on Parameter-Optimized Quantitative Structural Models (AdQSM). *Forests* **2023**, *14*, 475. [\[CrossRef\]](#)
62. Jiao, Y.; Wang, D.; Yao, X.; Wang, S.; Chi, T.; Meng, Y. Forest Emissions Reduction Assessment Using Optical Satellite Imagery and Space LiDAR Fusion for Carbon Stock Estimation. *Remote Sens.* **2023**, *15*, 1410. [\[CrossRef\]](#)
63. Schmidt, M.; Lucas, R.; Bunting, P.; Verbesselt, J.; Armston, J. Multi-Resolution Time Series Imagery for Forest Disturbance and Regrowth Monitoring in Queensland, Australia. *Remote Sens. Environ.* **2015**, *158*, 156–168. [\[CrossRef\]](#)
64. Rodríguez-Fernández, N.; Al Bitar, A.; Colliander, A.; Zhao, T. Soil Moisture Remote Sensing across Scales. *Remote Sens.* **2019**, *11*, 190. [\[CrossRef\]](#)
65. Wang, C.; Feng, M.-C.; Yang, W.-D.; Ding, G.-W.; Sun, H.; Liang, Z.-Y.; Xie, Y.-K.; Qiao, X.-X. Impact of Spectral Saturation on Leaf Area Index and Aboveground Biomass Estimation of Winter Wheat. *Spectrosc. Lett.* **2016**, *49*, 241–248. [\[CrossRef\]](#)
66. Jin, S.; Sun, X.; Wu, F.; Su, Y.; Li, Y.; Song, S.; Xu, K.; Ma, Q.; Baret, F.; Jiang, D.; et al. Lidar Sheds New Light on Plant Phenomics for Plant Breeding and Management: Recent Advances and Future Prospects. *ISPRS J. Photogramm. Remote Sens.* **2021**, *171*, 202–223. [\[CrossRef\]](#)
67. Coops, N.C.; Tompalski, P.; Goodbody, T.R.H.; Queinnec, M.; Luther, J.E.; Bolton, D.K.; White, J.C.; Wulder, M.A.; van Lier, O.R.; Hermosilla, T. Modelling Lidar-Derived Estimates of Forest Attributes over Space and Time: A Review of Approaches and Future Trends. *Remote Sens. Environ.* **2021**, *260*, 112477. [\[CrossRef\]](#)
68. Schlund, M.; Scipal, K.; Quegan, S. Assessment of a Power Law Relationship Between P-Band SAR Backscatter and Aboveground Biomass and Its Implications for BIOMASS Mission Performance. *IEEE J. Sel. Top. Appl. Earth Obs. Remote Sens.* **2018**, *11*, 3538–3547. [\[CrossRef\]](#)
69. Yang, Q.; Su, Y.; Hu, T.; Jin, S.; Liu, X.; Niu, C.; Liu, Z.; Kelly, M.; Wei, J.; Guo, Q. Allometry-Based Estimation of Forest Aboveground Biomass Combining LiDAR Canopy Height Attributes and Optical Spectral Indexes. *For. Ecosyst.* **2022**, *9*, 100059. [\[CrossRef\]](#)
70. Rius, M.; Darling, J.A. How Important Is Intraspecific Genetic Admixture to the Success of Colonising Populations? *Trends Ecol. Evol.* **2014**, *29*, 233–242. [\[CrossRef\]](#)
71. Blaschke, T. Object Based Image Analysis for Remote Sensing. *ISPRS J. Photogramm. Remote Sens.* **2010**, *65*, 2–16. [\[CrossRef\]](#)
72. Duro, D.C.; Franklin, S.E.; Dubé, M.G. A Comparison of Pixel-Based and Object-Based Image Analysis with Selected Machine Learning Algorithms for the Classification of Agricultural Landscapes Using SPOT-5 HRG Imagery. *Remote Sens. Environ.* **2012**, *118*, 259–272. [\[CrossRef\]](#)

Disclaimer/Publisher’s Note: The statements, opinions and data contained in all publications are solely those of the individual author(s) and contributor(s) and not of MDPI and/or the editor(s). MDPI and/or the editor(s) disclaim responsibility for any injury to people or property resulting from any ideas, methods, instructions or products referred to in the content.